

# Envelope equations for the Rayleigh–Bénard–Poiseuille system. Part 2. Linear global modes in the case of two-dimensional non-uniform heating

By DENIS MARTINAND<sup>1,2†</sup>, PHILIPPE CARRIÈRE<sup>1</sup>  
AND PETER A. MONKEWITZ<sup>2</sup>

<sup>1</sup>Laboratoire de Mécanique des Fluides et d'Acoustique, UMR CNRS 5509, Ecole Centrale de  
Lyon-Université Claude Bernard Lyon I-NSA Lyon BP163, 69131 Ecully cedex, France

<sup>2</sup>Laboratoire de Mécanique des Fluides, Ecole Polytechnique Fédérale de Lausanne,  
CH-1015, Lausanne, Switzerland

(Received 7 March 2003 and in revised form 21 October 2003)

Linear global modes in the Rayleigh–Bénard–Poiseuille system, for the case of two-dimensional non-uniform heating in the form of a single hot spot, are analysed in the framework of the envelope equation formalism. Global mode solutions are sought by means of WKBJ asymptotics. As for the one-dimensional case, an analytical selection criterion for the frequency may be derived from the breakdown of the WKBJ expansion at a two-dimensional double turning point located at the maximum of the local Rayleigh number. The analytical results, including the behaviour of the mode in the vicinity of the turning point, are compared with results obtained from numerical simulations of the envelope equation. Finally, the issue of the selection of the wavevector branches in the WKBJ expansion is discussed.

---

## 1. Setting up the spatially non-uniform problem

The Ginzburg–Landau equation with an advection term and variable coefficients has served widely as a model equation for the study of synchronized one-dimensional global modes (see Huerre & Monkewitz 1990; Chomaz, Huerre & Redekopp 1991; Le Dizès *et al.* 1996; Pier, Huerre & Chomaz 2001, among others). A two-dimensional Ginzburg–Landau equation in Rayleigh–Bénard–Poiseuille (RBP) convection at low Reynolds numbers, that is the mixed convection in a horizontal fluid layer heated from below with a superimposed one-directional Poiseuille through-flow, has been rigorously derived by envelope formalism in Part 1 of this paper (Carrière, Monkewitz & Martinand 2004, hereinafter referred to as I; equation numbers preceded by I refer to Part 1). The complex envelope  $A$  of transverse roll (TR) patterns, i.e. with the axes of the rolls perpendicular to the Poiseuille flow, in particular, is governed by equation (I3.20), with  $\cos \phi = 1$ :

$$\partial_t A = (r - \rho^2)A - \rho(c + \eta)\partial_x A + i\rho\eta\partial_y^2 A + (\partial_x - i\partial_y^2)^2 A - A^2\bar{A}, \quad (1.1)$$

† Present address: Turbulence and Mixing Group, Department of Aeronautics, Imperial College London, London SW7 2BY, UK.

where  $t$  denotes time and  $x$  and  $y$  the streamwise and transverse coordinates, respectively. The entire analysis and discussion in the present paper will be carried out in the coordinates defined in I, which have been scaled and transformed according to (I3.2)–(I3.3) and (I3.6). It suffices to recall here that the main characteristic of these coordinate definitions is the scaling of  $y$  like  $x^{1/2}$ . The transformed coordinates serve to simplify the presentation as much as possible, but, as a consequence, the recovery of the global mode envelope in physical coordinates is somewhat involved. The real control parameters  $r$  and  $\rho$  are the rescaled Rayleigh and Reynolds numbers, respectively, while  $c$  and  $\eta$  are two positive (real) functions of the Prandtl number  $P$ . In the case of spatially uniform  $r$  and  $\rho$ , the threshold for convective instability is obtained from the linearized version of (1.1) as  $r_c = \rho^2$ ; the boundary of absolute instability is  $r_a = \rho^2(1 + (c + \eta)^2/4)$  (see I3.23).

To understand the relation between the instability of a spatially uniform (parallel) system and localized instabilities associated with spatial non-uniformities, it is useful to start with the simplest possible model. It consists of keeping the rolls homogeneous in the  $y$ -direction parallel to their axes, i.e.  $\partial_y \equiv 0$  in (1.1), and confining the solution to a domain of finite streamwise extent by requiring  $A = 0$  at the boundaries  $x = 0$  and  $x = L$ , while keeping  $r$  and  $\rho$  constant. In this case, the marginally unstable solutions of the linearized version of (1.1) are  $A = \sin(n\pi x/L) \exp(\rho(c + \eta)/2)$ , and the corresponding critical values of the Rayleigh number are

$$r_c^{(n,L)} = \rho^2 \left( 1 + \frac{(c + \eta)^2}{4} \right) + \frac{(n\pi)^2}{L^2}. \quad (1.2)$$

It is noteworthy that for  $L \rightarrow \infty$ ,  $r_c^{(n,L)} \rightarrow r_a$  so that only local absolute instability gives rise to linear instability in a streamwise confined domain. However, as  $r$  exceeds the lowest  $r_c^{(1,L)}$ , modes with increasingly larger  $n$  become unstable and the solution develops strong gradients near the domain boundaries as it grows nonlinearly, thereby violating the assumptions for the derivation of the envelope equation (1.1) (see also the analogous phenomenon in the Ginzburg–Landau model for vortex shedding from a finite length cylinder, discussed in § 3 of Albarède & Monkewitz 1992). Furthermore, vanishing perturbations at both domain boundaries are not very realistic physically: in an experiment, perturbations swept into the test section are difficult to minimize and at the outflow boundary they are often substantial.

These problems can be alleviated by assuming a spatial variation of the control parameters in an infinite domain in such a manner that the system is linearly stable everywhere, except in a region of finite extent. Assuming, for instance, the parabolic variation  $r = r^{(\max)} - x^2/L^2$  in (1.1) where the  $y$ -derivatives are still omitted, the critical value  $r_c^{(\max)}$  for linear instability is found to be

$$r_c^{(\max)} = \rho^2 \left( 1 + \frac{(c + \eta)^2}{4} \right) + \frac{1}{L}. \quad (1.3)$$

Again, equation (1.3) behaves like  $r_c^{(n,L)}$  in the limit of  $L \rightarrow \infty$ , i.e.  $r_c^{(\max)} \rightarrow r_a$ .

To represent physical reality, however, the spatial variation of the parameter  $r$  should mimic the experimental condition of a fully developed Poiseuille flow with constant temperature entering the differentially heated part of the apparatus. For this, fully analytical solutions of equation (1.1) reduced to its  $x$ -variation are no longer adequate for a realistic shape of  $r(x)$ . We have to resort to an asymptotic analysis based on matched WKB expansions as in Monkewitz, Huerre & Chomaz (1993), for instance. Within this framework, the selection criterion for the most unstable global

(synchronized and self-excited) mode is obtained from the matching of the WKBJ expansions through turning points.

For the RBP problem, a first analysis of this type has been carried out in Carrière & Monkewitz (2001) for a purely streamwise variation of the Rayleigh number, i.e. for the two-dimensional case with only one wave propagation direction. The present study aims at extending the ideas and asymptotic methods used in the classical two-dimensional global mode analysis to the RBP system with two wave-propagation directions, i.e. to the case where the Rayleigh number  $r(x, y)$  in the full two-dimensional equation (1.1) varies slowly in both the streamwise and transverse directions.

The inclusion of the transverse parameter variation in the analysis of a thermal convection system such as the RBP system is essential to arrive at a physically realistic model, since convection patterns are known to be very sensitive to the presence of lateral walls, for instance. We note in passing that the through-flow profile in any real RBP cell also varies with  $y$  near the lateral walls. Moreover, in real systems non-uniformities of the temperature, for instance, are hardly one-dimensional, as assumed in Carrière & Monkewitz (2001), but take the form of ‘hot spots’ of various shapes. It is the aim of the present analysis to elucidate the conditions for which such a ‘hot spot’ within an RBP cell leads to a localized convection roll pattern. The influence of sidewalls on the through-flow and on the roll pattern, however, will not be considered. This amounts to assuming that the lateral extent of the RBP cell is large compared to the size of the hot spot and that the physical sidewalls are located within zones of local stability, which may be compared to the ‘viscous sponges’ used near (outflow) boundaries in numerical analysis.

The following global mode analysis is based on the envelope equation (1.1), which offers an attractive alternative to the major complications of an analysis based on the original conservation equations. The main simplification is that it allows us to work with an explicit rather than an implicit (numerically defined) local dispersion relation. Furthermore, numerical solutions of equation (1.1) are easily obtained to compare with analytical predictions, in particular providing a good test for the mode selection criteria to be developed.

The material is organized as follows: §2 is devoted to the WKBJ approximations and a discussion of the associated turning points. Next, the frequency selection criterion for global modes, associated with a double turning point in two dimensions, is derived in §3. Analytical predictions of global mode frequency and growth rate as well as the envelope amplitude in the neighbourhood of the double turning point are then compared in §4 with numerical simulations of the envelope equation with hot spots in the form of Gaussian bumps introduced through the spatial variations of the reduced Rayleigh number  $r$ . The last section, finally, is devoted to a general discussion of the relevance of the global mode analysis, and touches on some aspects of the complete global mode construction which involves matching of outer WKBJ expansions (outer in both the  $x$ - and  $y$ -directions) and the inner solution in the turning point region.

## 2. WKBJ expansion

The linear global mode analysis is governed by the linearized version of (1.1):

$$\partial_t A = (r - \rho^2)A - \rho(c + \eta)\partial_x A + i\rho\eta\partial_y^2 A + (\partial_x - i\partial_y^2)^2 A. \quad (2.1)$$

As in our previous work for the two-dimensional (i.e. one-dimensional in terms of wave propagation direction) problem (see Carrière & Monkewitz 2001), the spatial inhomogeneities are imposed through the  $x$ - and  $y$ -dependence of the reduced Rayleigh number  $r$ . In order to obtain a well-posed global mode problem,  $r$  is taken to be at a subcritical value sufficiently far from a central region, where a single maximum is reached for  $x = y = 0$ . Local instability arises in (2.1) when  $r > \rho^2$ .

The presence of the fourth derivative in  $y$  prevents the analytical solution of (2.1) for meaningful variations of  $r$ . Assuming that  $r$  varies on a typical length scale much larger than  $O(1)$ , i.e. the cell height, the solution of (2.1) can be approximated by WKBJ expansion. For this, we introduce the coordinates  $X = \varepsilon x$  and  $Y = \varepsilon y$ , slow relative to the original  $x$  and  $y$  coordinates of (1.1) and assume that  $r = r(X, Y)$ . The WKBJ expansion of a perturbation with complex frequency  $\omega$  on the trivial steady-state solution of (2.1) can then be written in the form:

$$A(X, Y, t) = (A_0(X, Y, \omega) + \varepsilon A_1(X, Y, \omega) + O(\varepsilon^2)) \exp\left(\frac{i}{\varepsilon} \Phi(X, Y, \omega) - i\omega t\right). \quad (2.2)$$

As in the one-dimensional case, the frequency is *a priori* expanded as  $\omega = \omega_0 + \varepsilon \omega_1 + O(\varepsilon^2)$ . The necessity of this expansion will become clear in the construction of the global mode. The components of the wavevector in the  $x$ - and  $y$ -directions, hereinafter denoted as  $a(X, Y, \omega)$  and  $b(X, Y, \omega)$ , respectively, are related to the phase  $\Phi(X, Y, \omega)$  by:

$$a(X, Y, \omega) = \partial_X \Phi, \quad b(X, Y, \omega) = \partial_Y \Phi, \quad (2.3)$$

with the continuity condition:

$$\partial_Y a = \partial_X b. \quad (2.4)$$

Conversely,  $\Phi$  may be determined from  $a$  and  $b$  using:

$$\Phi(X, Y, \omega) = \int_0^X a(p, Y) dp + \int_0^Y b(0, q) dq = \int_0^X a(p, 0) dp + \int_0^Y b(X, q) dq, \quad (2.5)$$

where the arbitrary value of  $\Phi(0, 0, \omega)$  is taken to be 0. Introducing the WKBJ expansion (2.2) in (2.1), a local dispersion relation is recovered at leading order:

$$\omega = i(r - \rho^2) + \rho c \partial_X \Phi + \rho \eta (\partial_X \Phi + (\partial_Y \Phi)^2) - i(\partial_X \Phi + (\partial_Y \Phi)^2)^2, \quad (2.6)$$

or, equivalently, in terms of  $a$  and  $b$ :

$$\omega = i(r - \rho^2) + \rho c a + \rho \eta (a + b^2) - i(a + b^2)^2. \quad (2.7)$$

The two-dimensional local dispersion relation (2.6) is now a nonlinear first-order partial differential equation on  $\Phi$ . As in the one-dimensional case, (2.6), or equivalently (2.7) and (2.4), defines a complete family of solutions among which only some are physically relevant (namely those satisfying condition (2.9)). Following the general methodology in Monkewitz *et al.* (1993), the partial differential equation for  $A_0$  is obtained at  $O(\varepsilon)$  in the WKBJ expansion:

$$\partial_a \omega \partial_X A_0 + \partial_b \omega \partial_Y A_0 + A_0 \left( -i\omega_1 + \frac{1}{2} \partial_a^2 \omega \partial_X a + \frac{1}{2} \partial_b^2 \omega \partial_Y b + \frac{1}{2} \partial_a \partial_b \omega (\partial_Y a + \partial_X b) \right) = 0. \quad (2.8)$$

This equation breaks down where  $\partial_a \omega = \partial_b \omega = 0$ , i.e. when the group velocity vanishes. As far as the dispersion relation (2.7) is concerned, such a turning point for the amplitude equation (2.8) does exist in Fourier  $(a, b)$ -space. Inspired by the one-dimensional case, this turning point is assumed to govern the behaviour of the global mode. A local analysis around this turning point is thus required and will be carried

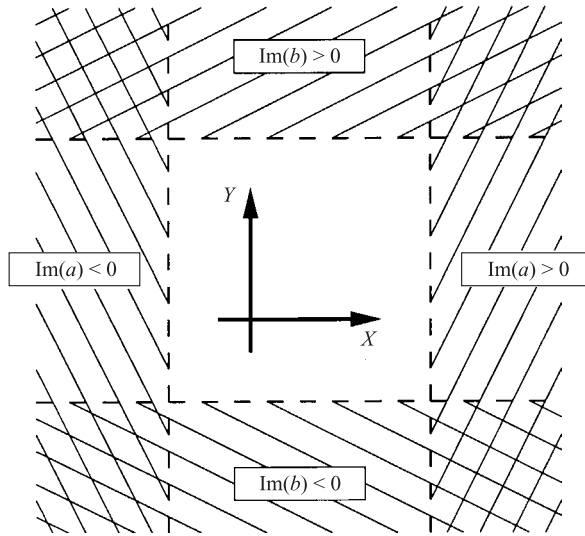


FIGURE 1. Regions of positive/negative imaginary parts of the wavenumbers  $a$  and  $b$  in the physical  $(X, Y)$ -space. Far from the central region,  $r$  has been assumed to correspond to regions of local stability.

out in §3. As in the one-dimensional case, the vanishing of the group velocity is related to branch changes of the wavevector, these branch changes being necessary to enforce the boundary conditions for the global mode. The subcritical values of  $r(x, y)$  sufficiently far from the central region require  $A(X, Y, t)$  to be bounded as  $|X| \rightarrow \infty$  or  $|Y| \rightarrow \infty$ . Thus,  $\Phi$  has to satisfy:

$$\text{Im}(\Phi(X, Y, \omega)) \rightarrow +\infty \text{ as } |X| \rightarrow \infty \text{ or } |Y| \rightarrow \infty. \tag{2.9}$$

Condition (2.9) may be equivalently expressed as:

$$\forall Y, \text{Im}(a) < 0 \text{ as } X \rightarrow -\infty, \quad \text{Im}(a) > 0 \text{ as } X \rightarrow +\infty, \tag{2.10a}$$

$$\forall X, \text{Im}(b) < 0 \text{ as } Y \rightarrow -\infty, \quad \text{Im}(b) > 0 \text{ as } Y \rightarrow +\infty, \tag{2.10b}$$

assuming the complex nature of  $a$  and  $b$ . The main difficulty in the calculation of the WKBJ expansion is that the group velocity and the wavevector have two components. The simultaneous treatment of the branch changes for both components of the wavevector is required to uniquely express and evaluate the first order of the WKBJ expansion (2.2). This implies that the decay of the global mode far from the locally unstable area should be considered in both the  $x$ - and  $y$ -direction, leading to the far-field values of the imaginary parts of  $a$  and  $b$  shown in figure 1. These requirements on the imaginary parts must be added to the required existence of several solution branches for  $a$  and  $b$ . The matchings of the different solution branches for  $a$  or  $b$  will be the main topic of §5.

### 3. The double turning point region

A turning point is defined by the conditions:

$$\partial_a \omega = \partial_b \omega = 0. \tag{3.1}$$

This turning point is two-dimensional by nature, and the two equations of (3.1) define a simple two-dimensional turning point. Together with (2.7), (3.1) defines the values

$\omega^t$ ,  $a^t$  and  $b^t$  at a turning point, identified by the superscript t. From

$$\rho(c + \eta) - 2i(a^t + b^{t^2}) = 0 \quad (3.2a)$$

and

$$2b^t(\rho\eta - 2i(a^t + b^{t^2})) = 0, \quad (3.2b)$$

it follows that:

$$a^t = -\frac{1}{2}i\rho(c + \eta), \quad b^t = 0, \quad (3.3)$$

and the local value of the frequency at this turning point is finally obtained as:

$$\omega^t = ir^t - i\rho^2 \left( 1 + \frac{(c + \eta)^2}{4} \right) = i(r^t - r_a), \quad (3.4)$$

where the local critical value for absolute instability  $r_a$  is given by (I3.23). As discussed in Le Dizès *et al.* (1996), the selection criterion could at this point be imposed by a set of simple turning points with a common value of  $r$  or by the coalescence of these turning points in a double turning point. The location  $(X^t, Y^t)$  of such a double two-dimensional turning point is defined by (3.1) and, in addition,

$$\partial_X \omega^t = \partial_Y \omega^t = 0. \quad (3.5)$$

The parametric dependence of  $\omega^t$  on  $X$  and  $Y$  via  $r^t(x, y)$  implies that the double turning point is located at the maximum of  $r^t$ , i.e. at

$$X^t = Y^t = 0. \quad (3.6)$$

As  $\text{Im}(\omega^t)$  is proportional to  $r^t$ , the local growth rate is largest at the double turning point. Therefore, it is reasonable to assume that this double turning point provides the selection criterion for the global mode. Possible global modes associated with a set of simple turning points will not be considered in this study.

In a direct extension of the one-dimensional case (see Huerre & Monkewitz 1990), two inner variables  $\chi = \varepsilon^{-1/2}X$  and  $\nu = \varepsilon^{-1/2}Y$  are introduced in the vicinity of the double turning point, and the perturbation is sought in the form:

$$A(\chi, \nu, t) = (A_0(\chi, \nu) + \varepsilon^{1/2}A_{1/2}(\chi, \nu) + \varepsilon A_1(\chi, \nu) + O(\varepsilon^{3/2})) \times \exp\left(\frac{i}{\varepsilon^{1/2}}(a^t\chi + b^t\nu) - i(\omega_0 + \varepsilon\omega_1)t\right), \quad (3.7)$$

while  $r$  is expanded as:

$$r = r^t + \frac{1}{2}\varepsilon(\partial_X^2 r^t \chi^2 + \partial_Y^2 r^t \nu^2 + 2\partial_X \partial_Y r^t \chi \nu) + O(\varepsilon^{3/2}). \quad (3.8)$$

For  $r$  to have a true maximum at the origin, we must assume that:

$$\partial_X^2 r^t < 0, \quad \partial_Y^2 r^t < 0 \quad \text{and} \quad (\partial_X \partial_Y r^t)^2 < \partial_X^2 r^t \partial_Y^2 r^t. \quad (3.9)$$

Inserting the expansions (3.7) and (3.8) into the governing equation (2.1), the homogeneous problem is recovered at  $O(\varepsilon^0)$ . Furthermore, the dispersion relation (2.7) implies  $\omega_0 = \omega^t$ . At  $O(\varepsilon^{1/2})$ , the stability equation is satisfied without loss of generality by  $A_{1/2} = 0$  while, at  $O(\varepsilon)$ , the following second-order partial differential equation for  $A_0$  is obtained:

$$\partial_X^2 A_0 - i\rho c \partial_\nu^2 A_0 + A_0(i\omega_1 + \frac{1}{2}(\chi^2 \partial_X^2 r^t + \nu^2 \partial_Y^2 r^t + 2\chi\nu \partial_X \partial_Y r^t)) = 0. \quad (3.10)$$

It is seen that separation of variables is possible in (3.10) if the principal axes of the temperature bump are aligned with the coordinates, i.e. in cases where  $\partial_X \partial_Y r^t = 0$ .

In this situation, the selection criterion and envelope equation become identical to the one-dimensional case (see Carrière & Monkewitz 2001). More general solutions for swept hot spots can be found by first introducing the substitution:

$$A_0 = F(\chi, \nu) \exp\left(-\frac{1}{2}(\alpha\chi^2 + \beta\nu^2 + 2\delta\chi\nu)\right). \quad (3.11)$$

The  $\alpha$ ,  $\beta$  and  $\delta$  in (3.11) are solutions of:

$$-\alpha^2 + i\rho c\delta^2 = \frac{1}{2}\partial_\chi^2 r^t, \quad (3.12a)$$

$$i\rho c\beta^2 - \delta^2 = \frac{1}{2}\partial_\nu^2 r^t, \quad (3.12b)$$

$$(-\alpha + i\rho c\beta)\delta = \frac{1}{2}\partial_\chi\partial_\nu r^t. \quad (3.12c)$$

Thus, the governing equation for  $F$  is:

$$\partial_\chi^2 F - i\rho c\partial_\nu^2 F - 2(\alpha\chi + \delta\nu)\partial_\chi F + 2i\rho c(\beta\nu + \delta\chi)\partial_\nu F + F(i\omega_1 + i\rho c\beta - \alpha) = 0. \quad (3.13)$$

For  $\omega_1 = -i\alpha - \rho c\beta$ , (3.13) has the particular solution  $F = \text{const}$ . Introducing the substitution:

$$\zeta = d\chi^2 + e\nu^2 + 2\delta\chi\nu, \quad (3.14)$$

with  $d$  and  $e$  given by:

$$de = \delta^2, \quad (3.15a)$$

$$id - \rho ce = i\alpha - \rho c\beta, \quad (3.15b)$$

equation (3.13) is transformed into an equation of the degenerate hypergeometric kind (see Polyanin & Zaitsev 1995, equation 2.1.2.103, p. 143)) for  $F(\zeta)$ :

$$(id + \rho ce)\zeta d_\zeta^2 F - \frac{1}{2}(2(id + \rho c\beta)\zeta - id - \rho ce)d_\zeta F - \frac{1}{4}(\omega_1 + i\alpha + \rho c\beta)F = 0. \quad (3.16)$$

Note that the system (3.15) generally has two solutions  $(d_1, e_1)$  and  $(d_2, e_2)$  for given values of  $\alpha$ ,  $\beta$  and  $\delta$ , thereby generating two independent variables  $\zeta_1$  and  $\zeta_2$  (corresponding to the independence of the original variables  $\chi$  and  $\nu$ ). Focusing on one variable  $\zeta$  and omitting the subscript, the solution of (3.16) is given by:

$$F(\zeta) = C_1 M\left(\alpha, \frac{1}{2}, \frac{\zeta}{\lambda}\right) + C_2 \left(\frac{\zeta}{\lambda}\right)^{1/2} M\left(\alpha + \frac{1}{2}, \frac{3}{2}, \frac{\zeta}{\lambda}\right), \quad (3.17)$$

with  $C_1$  and  $C_2$  two free constants,

$$\alpha = \frac{1}{4} \frac{\omega_1 + i\alpha + \rho c\beta}{id + \rho c\beta}, \quad \lambda = \frac{id + \rho ce}{id + \rho c\beta} \quad (3.18)$$

and  $M$  being the Kummer function (see Abramovitz & Stegun 1964).

The two-dimensional function  $F(\chi, \nu)$  is thus transformed into the sum of two independent one-dimensional functions  $F_1(\zeta_1)$  and  $F_2(\zeta_2)$  which can be studied in a similar fashion to the one-dimensional case (see, again, Huerre & Monkewitz 1990; Carrière & Monkewitz 2001). The decay of the global mode as  $|x| \rightarrow \infty$  or  $|y| \rightarrow \infty$  requires that  $A_0$  is a decaying function of  $|\chi|$  and  $|\nu|$ . A solution  $(\alpha_+, \beta_+, \delta_+)$  of (3.12) consistent with this requirement has to satisfy:

$$\text{Re}(\alpha_+) > 0, \quad \text{Re}(\beta_+) > 0, \quad \text{Re}(\delta_+)^2 < \text{Re}(\alpha_+)\text{Re}(\beta_+). \quad (3.19)$$

Moreover, for large  $|\zeta|$ , the Kummer function  $M$  increases more rapidly than the exponential term of (3.11) except when it reduces to Hermite polynomials. This is the

case when  $2a = -n$ , with  $n$  zero or a positive integer. Hence, the following relation is obtained for the  $O(\varepsilon)$  frequency

$$\omega_1^{(1,2)} = -i\alpha_+ - \rho c\beta_+ + 2n(id_{1,2} + \rho c\beta_+). \quad (3.20)$$

This defines two infinite sets of global modes in the directions  $\zeta_1$  and  $\zeta_2$  given by  $d_1$  and  $d_2$ , respectively, which correspond to a discrete frequency spectra. The two sets are connected at  $n=0$ , where the two solutions  $d_1$  and  $d_2$  coalesce. Equations (3.12), (3.15) and (3.17), together with conditions (3.9) and the conditions (3.19) of global mode decay far from the origin, finally yield the inner solution (3.11) and the associated complex frequency correction (3.20). Its consistency with the underlying mathematical construction of the global mode and its physical relevance are discussed next.

First, since the scale of the spatial variations of Hermite polynomials decreases with  $n$ , the mode number  $n$  cannot be too large without conflicting with the hypothesis of the slow  $O(\varepsilon^{1/2})$  variation of  $A_0(\chi, \nu)$ , as already remarked by Huerre & Monkewitz (1990). More specifically, for large  $n$ , the scaling of the inner region would have to be adapted to the faster variation of the solution, leading eventually to a situation of two first-order turning points separated by an  $O(\varepsilon^0)$  distance, as considered by Le Dizès *et al.* (1996). Whether the modes with large  $n$  are physically relevant, depends on the sign of the imaginary part of  $2n(id_{1,2} + \rho c\beta_+)$  in (3.20). Since our analysis breaks down for large  $n$ , we clearly require that

$$\text{Im}(id_{1,2} + \rho c\beta_+) < 0, \quad (3.21)$$

which makes the mode  $n=0$  the most unstable, or critical, mode. It is not clear whether condition (3.21) can be derived in any generality from fundamental principles, but we are not aware of any global mode computation where this condition is violated for realistic flow. In other words, it appears that, in practice, the most unstable global mode is the one with the simplest spatial structure.

Next, we invoke heuristic arguments to fix the sign of the imaginary part of the frequency correction (3.20), i.e. the difference between the global growth rate and the maximum local absolute growth rate at the top of the temperature bump. Specifically, we require that critical global mode  $n=0$  grows at a smaller rate than the maximum local absolute growth rate, i.e that  $\text{Im}(\omega_1) < 0$  for all  $n$ , including  $n=0$ . For this, it is sufficient to require, in addition to (3.21) that

$$\text{Im}(-i\alpha_+ - \rho c\beta_+) < 0. \quad (3.22)$$

This condition is motivated by the intuitive physical argument that in the inhomogeneous system, the regions far from the ‘hot spot’ must be entrained by the most unstable local mode dominating at the top of the temperature bump. It is reasonable to expect that this entrainment or synchronization of the mismatched – more stable – outer regions causes additional radiation and/or viscous losses to the most unstable local mode at the top of the temperature bump, compared to the homogeneous situation without mismatched outer regions where the mean flow is everywhere equal to the most absolutely unstable mean flow at the top of the temperature bump†. If we assume that the inhomogeneity does not reinforce the

† A similar ‘transmission loss’ argument appears to be valid in the case of a single spatial instability wave propagating in a slowly varying inhomogeneous medium (see e.g. Crighton & Gaster 1976; Gaster, Kit & Wagnanski 1985), where in all the known examples, the total spatial amplification is reduced when carrying the WKB approximation from the level of ‘geometrical

destabilization mechanism relative to the parallel case, the postulated loss translates into  $\text{Im}(\omega_1) < 0$  for all  $n$ . Another way of justifying (3.22) is to consider the consequences of  $\text{Im}(\omega_1) > 0$  for, say, the critical mode  $n=0$ : in this case, the global growth rate to  $O(\varepsilon^1)$ ,  $\text{Im}(\omega_0 + \varepsilon\omega_1)$  would increase with increasing non-parallelism  $\varepsilon$  while keeping  $\omega_0$  fixed. In other words, the global growth rate would be increased by reducing the size of the hot spot while keeping the conditions at its centre fixed. This is obviously unreasonable in the limit of small hot spots with relatively large  $\varepsilon$  of, say,  $O(1)$ . However, our  $O(\varepsilon^1)$  analysis does not apply to  $\varepsilon$  for which the argument is obvious and in the limit of small  $\varepsilon$  we were, again, not able to derive condition (3.22) from some fundamental principle. Nevertheless, we are not aware of any realistic flow in which the global growth rate has been found to exceed the maximum local absolute growth rate in the flow. In the symmetric example where  $\partial_x \partial_y r^t = 0$ , the coefficients satisfying (3.19) are given by

$$\alpha_+ = \left( \frac{-\partial_x^2 r^t}{2} \right)^{1/2}, \quad \beta_+ = \frac{1+i}{2} \left( \frac{-\partial_y^2 r^t}{\rho c} \right)^{1/2}, \quad d_1 = \alpha_+ + i\rho c\beta_+, \quad d_2 = 0. \quad (3.23)$$

This leads to:

$$-i\omega_1^{(1)} = -(2n+1) \left( \frac{-\partial_x^2 r^t}{2} \right)^{1/2} - \frac{1}{2}(-\rho c \partial_y^2 r^t)^{1/2} + \frac{i}{2}(-\rho c \partial_y^2 r^t)^{1/2}, \quad (3.24a)$$

$$-i\omega_1^{(2)} = - \left( \frac{-\partial_x^2 r^t}{2} \right)^{1/2} - \frac{2n+1}{2}(-\rho c \partial_y^2 r^t)^{1/2} + \frac{i(2n+1)}{2}(-\rho c \partial_y^2 r^t)^{1/2}. \quad (3.24b)$$

Thus, conditions (3.21) and (3.22) are satisfied and the most unstable global mode is the one with  $n=0$  and  $F = \text{const.}$ , i.e. with a Gaussian shape for the amplitude in both the  $\chi$ - and  $\nu$ -direction. In the case where  $\partial_x \partial_y r^t \neq 0$ , the solution is more complicated and explicitly given in Martinand (2003). Nevertheless, as stated above, it has not been established so far that conditions (3.21) and (3.22) flow from general properties of the dispersion relation (2.7) at the turning point, together with conditions (3.9) and (3.19). In the present study, we have analytically investigated the solutions of (3.20) for specific values of the parameters covering the range used in the numerical simulation of §4. In this range of parameter values, a single solution  $(\alpha_+, \beta_+, \delta_+)$  of system (3.12) was always found to satisfy condition (3.19). In agreement with the numerical simulations, this solution always induced the matching of conditions (3.21) and (3.22), with, consequently, the most unstable mode obtained for  $n=0$  and a stabilizing effect of the spatial variations of the reduced Rayleigh number.

As a last step, the selection criterion and the envelope are reexpressed in terms of original coordinates  $x$  and  $y$ . The correction at  $O(\varepsilon)$  for the frequency is then

$$\varepsilon\omega_1 = -i\varepsilon\alpha - \rho c\varepsilon\beta. \quad (3.25)$$

The envelope approximation in the inner region of the most unstable mode previously evaluated is

$$A_0(x, y) = \exp\left(-\frac{1}{2}(\varepsilon\alpha x^2 + \varepsilon\beta y^2 + 2\varepsilon\delta xy)\right), \quad (3.26)$$

optics', represented by the exponential factor in (2.2), to the level of 'physical optics', including the corrective factor  $A_0$  in (2.2). Note that in the 'geometrical optics' approximation, all the perturbation energy is transmitted downstream, while the mismatch of eigenfunctions between consecutive streamwise stations enters into the determination of  $A_0$ .

with  $\varepsilon\alpha$ ,  $\varepsilon\beta$  and  $\varepsilon\delta$  the solutions of the following system (3.27) satisfying conditions (3.19), which are checked to satisfy conditions (3.21) and (3.22).

$$-(\varepsilon\alpha)^2 + i\rho c(\varepsilon\delta)^2 = \frac{1}{2}\partial_x^2 r^t, \quad (3.27a)$$

$$i\rho c(\varepsilon\beta)^2 - (\varepsilon\delta)^2 = \frac{1}{2}\partial_y^2 r^t, \quad (3.27b)$$

$$(-\varepsilon\alpha + i\rho c\varepsilon\beta)\varepsilon\delta = \frac{1}{2}\partial_x\partial_y r^t. \quad (3.27c)$$

#### 4. Numerical simulations

In this section, the quality of the analytical description of the global mode developed in §3 is assessed by comparison with the linear growth stage of numerical solutions of the nonlinear equation (1.1). For this, we use a Prandtl number of  $P = 7$  corresponding to the coefficient values  $c = 11.27$  and  $\eta = 0.101$ , as derived in I (I2.11 and I2.13d modified by I3.19). Furthermore, the spatial variation of the parameter  $(r - \rho^2)(x, y)$  is assumed to be a two-dimensional Gaussian bump with, in the most general case, a swept elliptical planform:

$$(r - \rho^2)(x, y) = -1 + 2 \exp \left( -\frac{1}{2}x^2 \left( \frac{\cos^2 \psi}{\sigma_1^2} + \frac{\sin^2 \psi}{\sigma_2^2} \right) - \frac{1}{2}y^2 \left( \frac{\sin^2 \psi}{\sigma_1^2} + \frac{\cos^2 \psi}{\sigma_2^2} \right) - \frac{1}{2}xy \sin 2\psi \left( \frac{1}{\sigma_1^2} - \frac{1}{\sigma_2^2} \right) \right), \quad (4.1)$$

where  $\psi$  is the angle between the  $x$ -axis and the principal axis ‘1’ of characteristic length  $\sigma_1$ . For simplicity, the function  $(r - \rho^2)(x, y)$  is kept unchanged, while the reduced Reynolds number  $\rho$  is reduced below its critical value  $\rho_{\text{crit}}$  which therefore depends on  $\sigma_1$ ,  $\sigma_2$  and  $\psi$  only. The local stability properties are then best characterized in terms of  $(r - \rho^2)$ . Where  $(r - \rho^2)(x, y) < 0$  the system is locally stable (LS). For  $0 < (r - \rho^2)(x, y) < \rho^2(c + \eta)^2/4$ , the system is locally convectively unstable (LCU) and, finally, it is locally absolutely unstable (LAU) for  $(r - \rho^2)(x, y) > \rho^2(c + \eta)^2/4$ . As an LAU region is necessary to destabilize a global mode of the type considered here, the critical parameter  $\rho_{\text{crit}}$  must be smaller than  $\rho_a = 2/(c + \eta) = 0.1759$ .

The numerical calculations are performed in a square domain  $(x, y) \in [-50, 50; -50, 50]$  with a spatial mesh size of  $\Delta x = \Delta y = 0.5$ . A centred second-order spatial scheme is used on this grid and time is advanced by an explicit first-order Euler scheme with a time step of  $\Delta t = 2 \times 10^{-3}$ . When starting a numerical simulation from a white noise initial condition, the dominant eigenstate emerges only after a substantial transient. This transient growth does not affect the asymptotic behaviour of the numerical simulation as far as the final growth rate and eigenstate are concerned. This is particularly evident for a damped instability, where saturation does not alter the linear dynamics. As seen in figure 2(a), this transient corresponds in our system to a temporary increase of the mean perturbation energy by several orders of magnitude. The asymptotic behaviour being our only concern, it is desirable to eliminate this large transient. For this, the analytical expression (3.26) of the most amplified or least damped linear mode in the ‘summit’ region of the temperature bump, as obtained in §3, is used as the initial condition for the computation. Figure 2(b) clearly shows that this initial condition dramatically reduces the duration and magnitude of the transient growth (note the different vertical scales). As it should be, the asymptotic decay rate is the same in both cases, equal to  $4.2 \times 10^{-3}$ . Furthermore, the asymptotic perturbation (eigenstate) in figure 2(c) obtained from white noise is identical to the

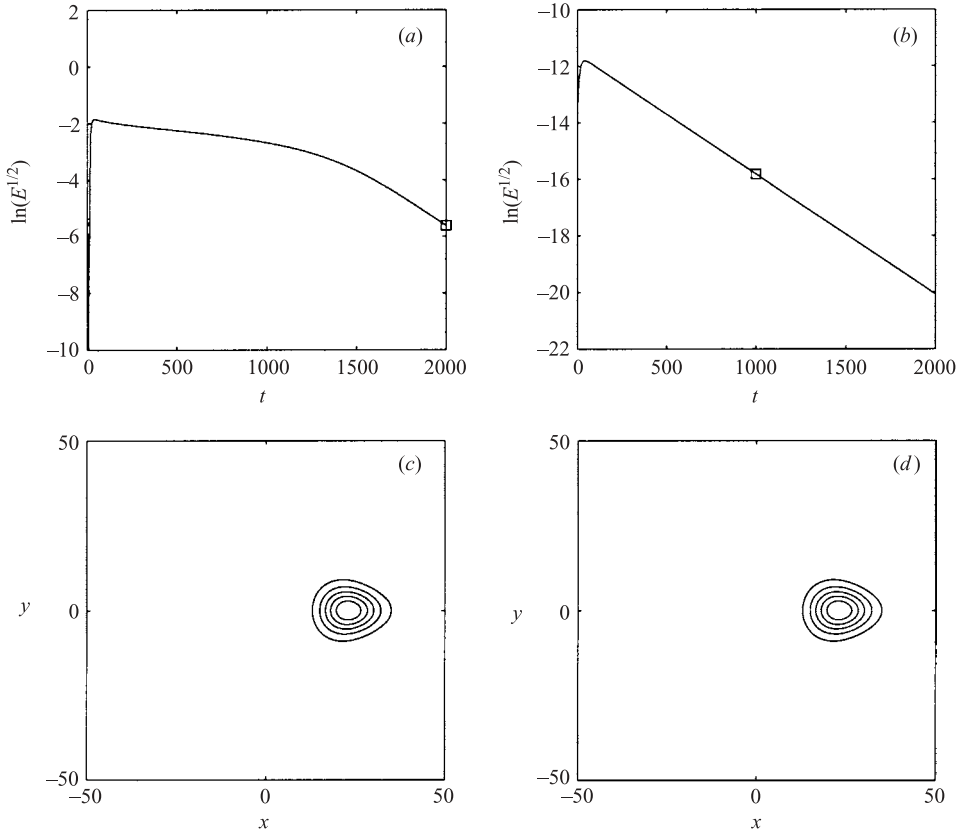


FIGURE 2. Comparison between the evolution of white noise (a) and (c) and of the dominant analytical mode (b) and (d), with an initial mean amplitude of  $10^{-6}$  in both cases.  $\sigma_1 = \sigma_2 = 20$  and  $\rho = 0.1627$ . The two top figures show the space-averaged amplitude and the times ( $\square$ ) of the amplitude ‘snapshots’ in the bottom figures.

perturbation in figure 2(d) obtained with analytical initial condition. For the circular bump of figure 2, this asymptotically dominant numerical eigenstate is egg-shaped with a gradually rising front and an advected downstream tail.

In unstable cases, the asymptotic saturated states are independent of the initial conditions, but are of minor interest as this long time behaviour is dominated by the nonlinear effects independently of the linear growth rate. The transient growth starting from white noise merges into the saturated state due to the nonlinear term of (1.1) before the exponentially growing dominant linear eigenmode can emerge by selective amplification. This purely exponential growth, which is the object of comparison, can only be isolated by initiating the simulations with the analytical mode.

To further test the global mode analysis in §3, the analytical and numerical values for the critical Reynolds number  $\rho_{\text{crit}}$  are compared. The analytical  $\rho_{\text{crit}}^{\text{ana}}$  is obtained by finding the zero of the function  $\text{Im}(\omega = \omega^l + \omega_1)$  of  $\rho$  (cf. (3.4) and (3.25)) for the given bump shape  $(r - \rho^2)(x, y)$ . The numerical value  $\rho_{\text{crit}}^{\text{num}}$  is extrapolated from the linear growth rates of the envelope amplitude at the centre of the cell for three unstable values of  $\rho$  and the same  $(r - \rho^2)(x, y)$  function, as shown in figure 3.

Next, the numerical and analytical envelope fields for a given set of parameters  $\sigma_1, \sigma_2, \psi$  and  $\rho$  are compared. Using (3.26), (3.3), (3.4) and (3.25), the envelope field is

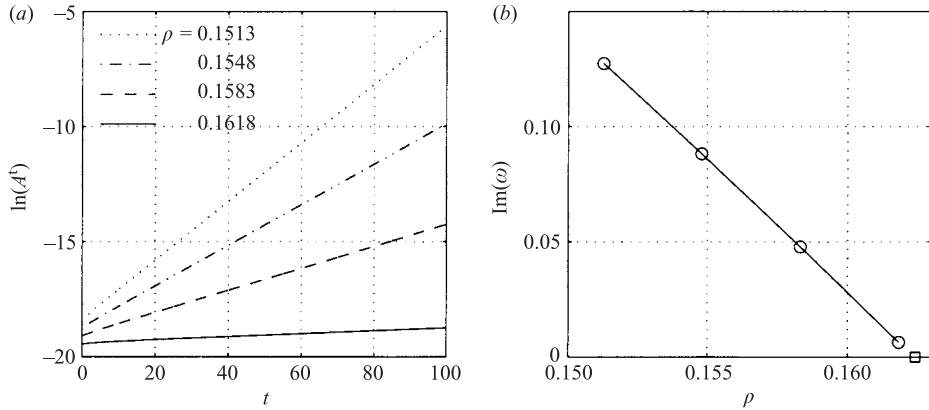


FIGURE 3. Evaluation of the numerical  $\rho_{\text{crit}}^{\text{num}}$  for  $\sigma_1 = \sigma_2 = 20$ . (a) Evolution of the amplitude at the centre of the cell for different values of  $\rho$ . (b) Growth rates ( $\circ$ ) extracted from (a) with linear extrapolation to  $\rho_{\text{crit}}^{\text{num}} = 0.1624$  ( $\square$ ).

analytically approximated by the expression for the envelope of the most unstable global mode in the double turning-point region:

$$A(x, y) = A_0(x, y) \exp(ia^t x + ib^t y - i(\omega^t + \varepsilon \omega_1)t). \quad (4.2)$$

This analytical expression of the envelope does not incorporate the WKBJ expansion and variation of the wave vector far from the temperature bump ‘summit’.

The bump (4.1) is characterized by three geometrical features: its characteristic size, its aspect ratio and its angle  $\psi$  with the  $x$ -axis. The first feature is investigated with circular bumps of variable size. The second one is investigated with symmetric bumps with constant  $\sigma_1 \sigma_2$  and variable aspect ratio. The last dependency is investigated with bumps of fixed aspect ratio and variable sweep angle.

#### 4.1. Circular bumps with variable unstable area

As  $\sigma = \sigma_1 = \sigma_2$  is increased, the analytical and numerical critical values of  $\rho$  increase and the convective–absolute threshold  $\rho_a$  is approached, as expected when the size of the unstable domain is increased. As seen in figure 4, the agreement between the numerical simulations and the selection criterion is good. For small values of  $\sigma$ , the analytical assumption of slow spatial variations of (4.1) is barely satisfied and the agreement between numerical and analytical results deteriorates, the latter underpredicting  $\rho_{\text{crit}}$ . For large values of  $\sigma$ , the remaining small difference between the numerical and analytical results is due to the rather coarse mesh used for the numerical simulation. It was checked for  $\sigma = 20$ , that the refinement of this mesh, with a corresponding decrease of the time step to satisfy the CFL condition, makes  $\rho_{\text{crit}}^{\text{ana}}$  coincide with the limit of  $\rho_{\text{crit}}^{\text{num}}$  for zero mesh size.

Considering now the amplitude distribution, the locations of the roll packet just downstream of the LAU region are similar for the analytical approximation and the numerical simulation, but the two amplitude distributions are conspicuously different. As seen in figure 5, the peak of the analytical approximation is wider than in the numerical simulation, does not present an advected tail and its maximum is shifted upstream.

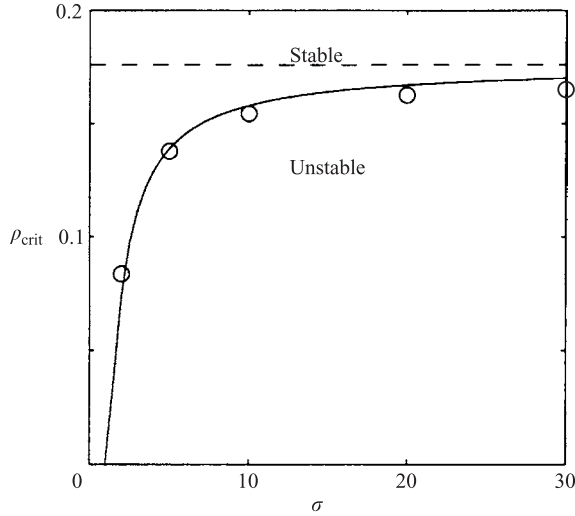


FIGURE 4. Comparison between analytical (—) and numerical (○) critical values of  $\rho$  versus the bump size  $\sigma = \sigma_1 = \sigma_2$ . The dashed line is the convective–absolute threshold  $\rho_a = 0.1759$  for the homogeneous case.

#### 4.2. Elliptical bumps with variable aspect ratio

The next step is to consider bumps with different aspect ratios  $\sigma_1/\sigma_2$  aligned with the  $x$ -direction. The analytical selection criterion is seen in figure 6 to agree well with the numerical results. We note that high and low values of  $\sigma_1/\sigma_2$  violate the assumption of slow variation. The effect is that low values of  $\sigma_2$  cause the selection criterion to overpredict the critical value of  $\rho$  whereas low values of  $\sigma_1$  lead to an underprediction. This discrepancy turns out to be severe for  $\varepsilon \sim O(1)$ . For  $\sigma_1 = 1$ , for instance, the system is analytically found to be always stable, i.e.  $\rho_{\text{crit}}^{\text{ana}} = 0$ , whereas it is numerically unstable below  $\rho_{\text{crit}}^{\text{num}} = 0.0777$ .

It is noteworthy that for a constant characteristic area of the unstable domain, the confinement effect in the  $y$ -direction is as stabilizing as the confinement in the  $x$ -direction, despite the advective effect of the mean flow that could be expected to stabilize preferentially bumps which are short in the  $x$ -direction. Hence, the most unstable situation is attained for the circular bump.

#### 4.3. Swept elliptical bumps

A swept elliptical bump completely breaks the symmetries in the  $y$ -direction and is therefore of interest to validate the selection criterion imposed by a double turning point at the top of the bump. As seen in figure 7, the analytical selection criterion agrees well with the numerical values of the threshold  $\rho_{\text{crit}}$  and provides the correct dependence on the sweep angle  $\psi$ . From figure 7, it is seen that  $\psi$  has only a strong effect on the oscillation period of the instability with  $\psi$ , as the variation of  $T$  is of the order of magnitude of the period, with a significant decrease when the bump is elongated in the  $x$ -direction. We also note that the agreement between analytical and numerical periods improves with the characteristic size of the bump in the  $x$ -direction, i.e. when  $\psi \rightarrow \pi/2$  in figure 7(b).

Concerning the envelope shape, the position of the global mode is well captured by the analysis. As seen in figure 8, the maximum of the envelope amplitude is located on the boundary between the LCU and LS regions, as for a global mode associated

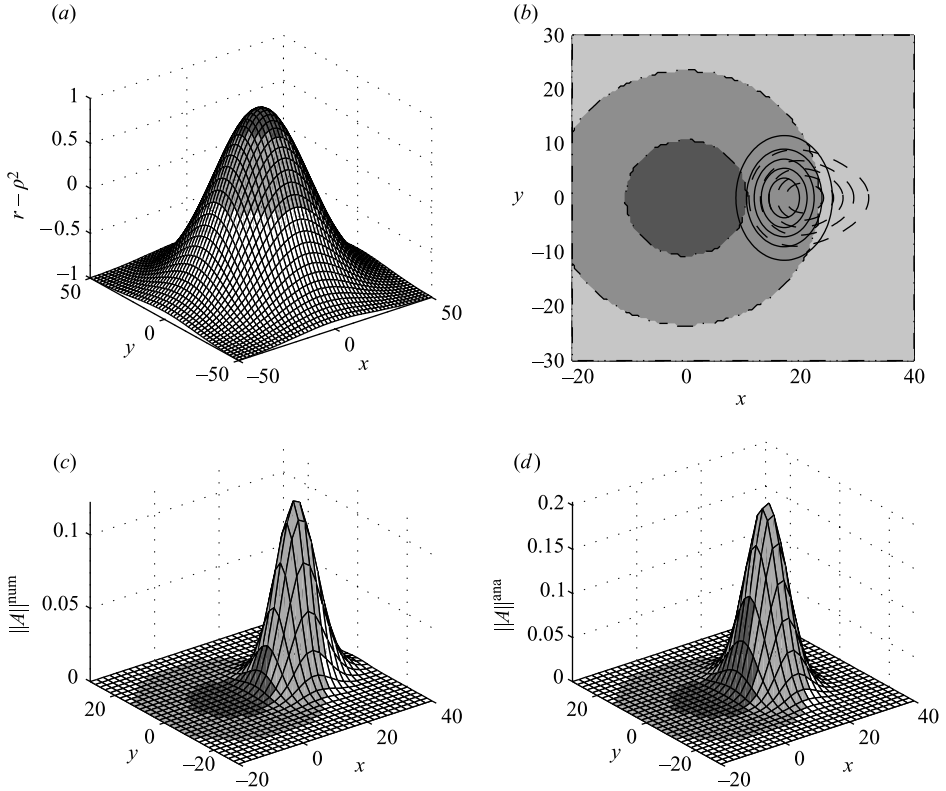


FIGURE 5. Comparison between analytical approximation and numerical simulation of the envelope amplitude, with  $\sigma_1 = \sigma_2 = 20$ ,  $\rho = 0.1513$ ,  $\varepsilon\alpha = 0.05$ ,  $\varepsilon\beta = 0.0272 + i0.0272$ ,  $\varepsilon\delta = 0$  and  $\omega = -0.0459 + i0.1816$ . The amplitudes are shown at  $t = 60$  where the initial mean amplitude is  $10^{-6}$  in both cases. (a)  $(r - \rho^2)$  as a function of  $x$  and  $y$ . (b) Comparison of analytical (—) and numerical (- -) amplitude contours. (c, d) Three-dimensional representations of numerical and analytical amplitudes, respectively. In the four figures, the darkest shade marks the LAU region, the intermediate shade the LCU region and the lightest shade the LS region.

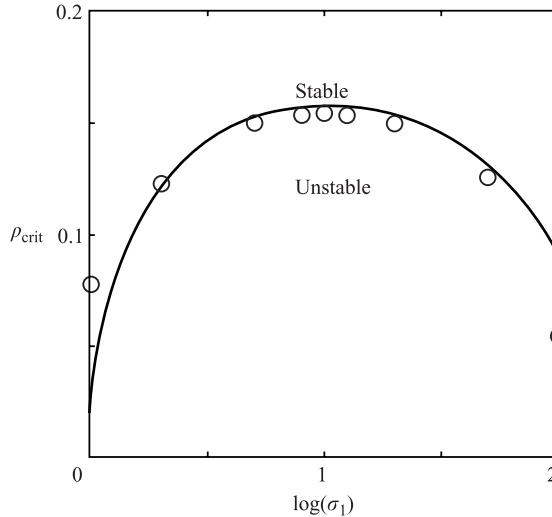


FIGURE 6. Comparison between analytical (—) and numerical (○) critical values of  $\rho$  as functions of  $\sigma_1$ , with  $\sigma_1\sigma_2 = 100$ .

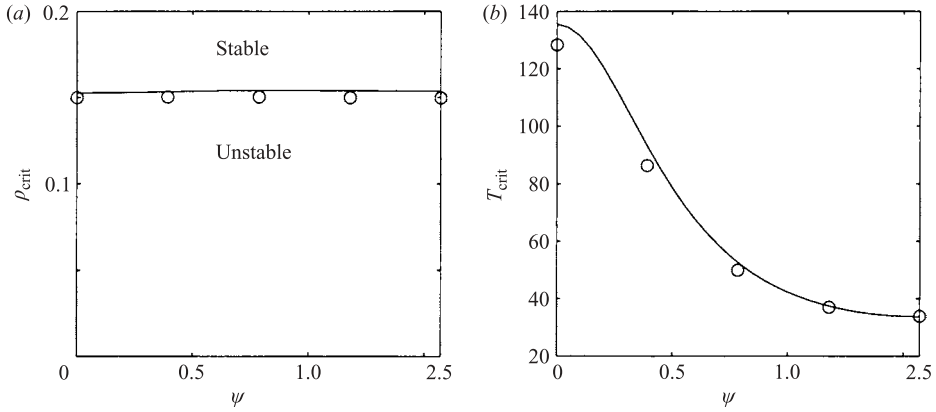


FIGURE 7. Comparison between (a) analytical (—) and numerical (○) critical values of  $\rho$  and (b) oscillation periods at the numerical and analytical stability threshold, respectively, as functions of  $\psi$  ( $\sigma_1 = 5$  and  $\sigma_2 = 20$ ).

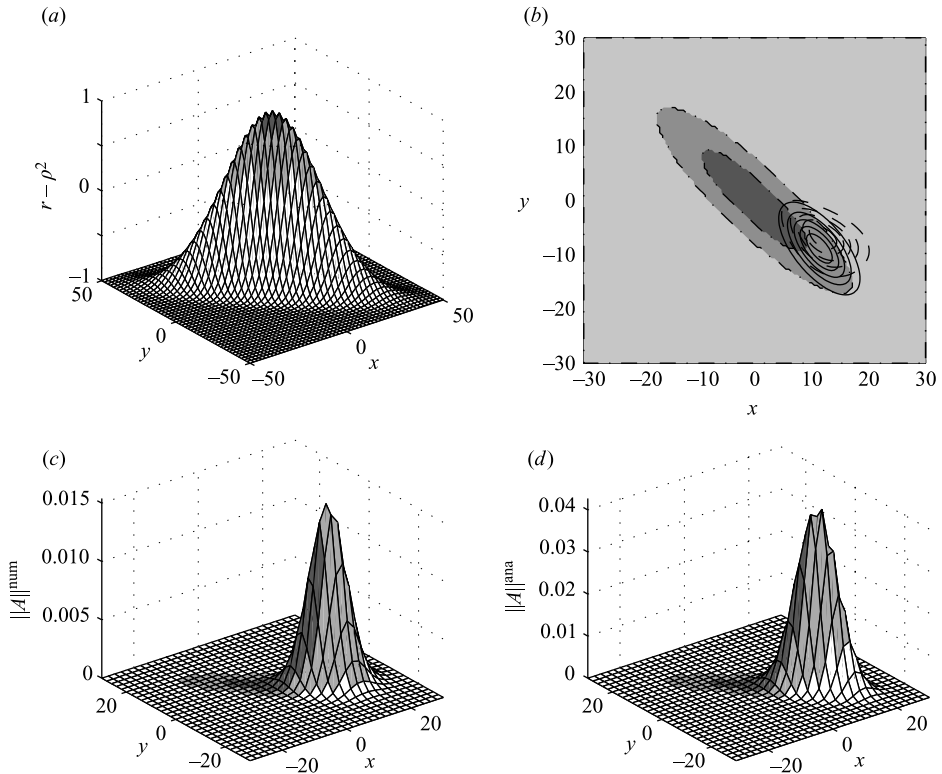


FIGURE 8. Comparison between analytical approximation and numerical simulation of the envelope amplitude, with  $\sigma_1 = 5$ ,  $\sigma_2 = 20$ ,  $\psi = \pi/4$ ,  $\rho = 0.1407$ ,  $\varepsilon\alpha = 0.1218 + i0.0214$ ,  $\varepsilon\beta = 0.0848 + i0.0668$ ,  $\varepsilon\delta = 0.0660 + i0.0328$  and  $\omega^\dagger + \varepsilon\omega_1 = -0.1131 + i0.1323$ . The other parameters and conventions are as in figure 5.

with a one-dimensional  $r(x)$  bump (see for instance Carrière & Monkewitz 2001). In the transverse direction, the maximum is located close to the most downstream point of the boundary between the LAU and LCU regions.

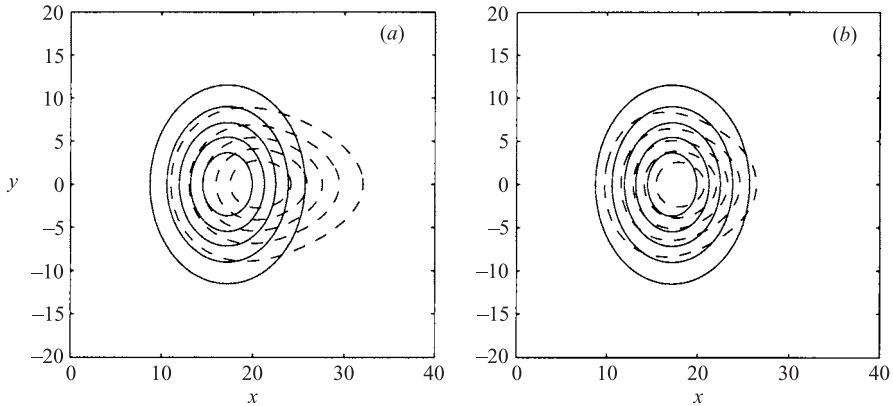


FIGURE 9. Comparison between the analytical approximation (—) and the numerical simulation (---) of the envelope amplitude using (a) a Gaussian and (b) a parabolic ( $r - \rho^2$ )-bump. The parameters are as in figure 5.

## 5. Discussion

Before discussing the relevance of the analytical approximation of the global mode and its possible improvements, the reader is again reminded that the  $x$  and  $y$  coordinates used here are scaled and transformed as specified in §3 of I. So again, the global mode shapes shown in this section do not correspond directly to the shapes that would be observed in physical space.

As shown in the previous section, in particular figures 4, 6 and 7, the frequency selection criterion obtained from the analytical approximation agrees well with the numerical simulations, provided  $\varepsilon$  is small. Furthermore, as this criterion derives directly from the dispersion relation, the global mode frequency and growth rates are relatively easy to evaluate. However, the inner region approximation (3.26), obtained from (3.10), yields only the general shape and location of the ‘convection roll packet’. A closer look at figures 5 and 8 reveals obvious differences between the analytical approximation and the numerical simulation discussed in the following.

A first consequence of extending the inner region solution (3.26) to the whole domain is that the coefficient  $(r - \rho^2)(x, y)$  in (3.10) behaves as the parabola (3.8) fitting the Gaussian bump (used for the computations) at its maximum. The further from the centre of the bump the rolls are, the more their degree of instability ( $r - \rho^2$ ) is underpredicted by the parabolic approximation. To investigate to what degree this difference is responsible for the larger downstream extent of the roll packet – the advected tail – in the numerical simulations, computations with the parabolic function (3.8) for  $(r - \rho^2)(x, y)$  have been carried out. As seen in figure 9, this partially reduces the downstream extent of the numerical global mode and moves the numerical and analytical amplitude maxima together.

To explain the remaining difference, it must be kept in mind that, according to the inner region asymptotics, the analytical wavevector  $(a, b)$  is equal to  $(a^i, b^i)$  everywhere in the domain, whereas the simulations use the full dependence of the wavenumbers on  $r$  for both the Gaussian and parabolic ( $r - \rho^2$ ) bumps. Improving the accuracy of the analytical approximation away from the top of the bump would require the WKBJ expansions in the outer regions where the wavenumbers vary with  $r$ . As stated in §2, the complete expression of the amplitude in the outer region requires the partial matching of expansions valid on different spatial branches of

$a$  or  $b$ . The main complication of these matchings is that the branch switching of one component of the wavevector depends on the other component. Since the complete WKB approximation of the wavevector field remains at the moment an open problem, we can only attempt to outline the issues at stake and raise the question of the integration of the outer solution. Specifically, the discussion will be limited to the matching of solution branches in the Fourier  $(a, b)$ -space, where we show how the global mode can be constructed in principle. The proposed construction blueprint may, however, not be unique and, furthermore, the translation of trajectories in  $(a, b)$ -space into WKB integration paths in the complex  $(X, Y)$ -space is far from trivial and may not be possible in some cases. Nevertheless, the numerical simulations suggest that the proposed global mode construction is possible for the examples in this paper.

With wave propagation in both the  $X$  and  $Y$  directions, the spatial branches of each component of the wavevector are surfaces parameterized by the other component, e.g.  $a(X, Y, b, \omega)$  and  $b(X, Y, a, \omega)$ . Considering the construction of a WKB solution outlined in §2 and §3, the calculation of the phase  $\Phi(X, Y)$  requires knowledge of where the wavevector has to switch from one solution surface of the dispersion relation to another. What has already been established is that the boundedness of the amplitude imposes on the imaginary parts of the wavevector components the conditions (2.10), summarized in figure 1. Unlike in the one-dimensional case, these conditions do not lead in a straightforward manner to the choice of the correct branch of the wavevector. With  $\omega$  given by the selection criterion at the double turning point, the dispersion relation (2.7) yields  $a$  as a function of  $b$ :

$$a_{\pm} = -b^2 - \frac{1}{2}i\rho(c + \eta) \pm (i\rho cb^2 - (r^t - r))^{1/2}. \quad (5.1)$$

The two solutions merge for  $\partial_a \omega = 0$ , i.e.  $i\rho cb^2 - (r^t - r) = 0$ , and the two associated branch points are:

$$a_{\text{bp1}} = i \left( \frac{r^t - r}{\rho c} - \frac{\rho}{2}(c + \eta) \right), \quad (5.2a)$$

$$b_{\text{bp1}} = \left( \frac{r^t - r}{2\rho c} \right)^{1/2} (1 - i), \quad (5.2b)$$

and

$$a_{\text{bp2}} = i \left( \frac{r^t - r}{\rho c} - \frac{\rho}{2}(c + \eta) \right), \quad (5.3a)$$

$$b_{\text{bp2}} = - \left( \frac{r^t - r}{2\rho c} \right)^{1/2} (1 - i). \quad (5.3b)$$

As depicted in figure 10, the branch cuts are chosen along the Stokes lines in the  $b$ -plane, satisfying  $\text{Im}(a_+) = \text{Im}(a_-)$  and joining  $b_{\text{bp1}}$  to  $b_{\text{bp2}}$  via infinity, so as to exclude the point  $b = 0$ . These branch cuts, on which the imaginary parts of  $a$  are folded and the real parts discontinuous, cannot be crossed by a path in  $(a, b)$ -space. Hence, we can only switch from one  $a$ -solution surface to the other through one of the branch points. A consequence of the choice of branch cuts in the  $b$ -plane is the relation  $\text{Im}(a_1) \geq \text{Im}(a_2)$ , where the ‘equal to’ sign applies only at the branch points. However,  $\text{Im}(a)$  can change sign on any given solution surface and the condition (2.10) is therefore not sufficient to determine the correct branch of  $a$  in the different regions of physical  $(X, Y)$ -space in figure 1. Progress can be made by considering  $b$  as

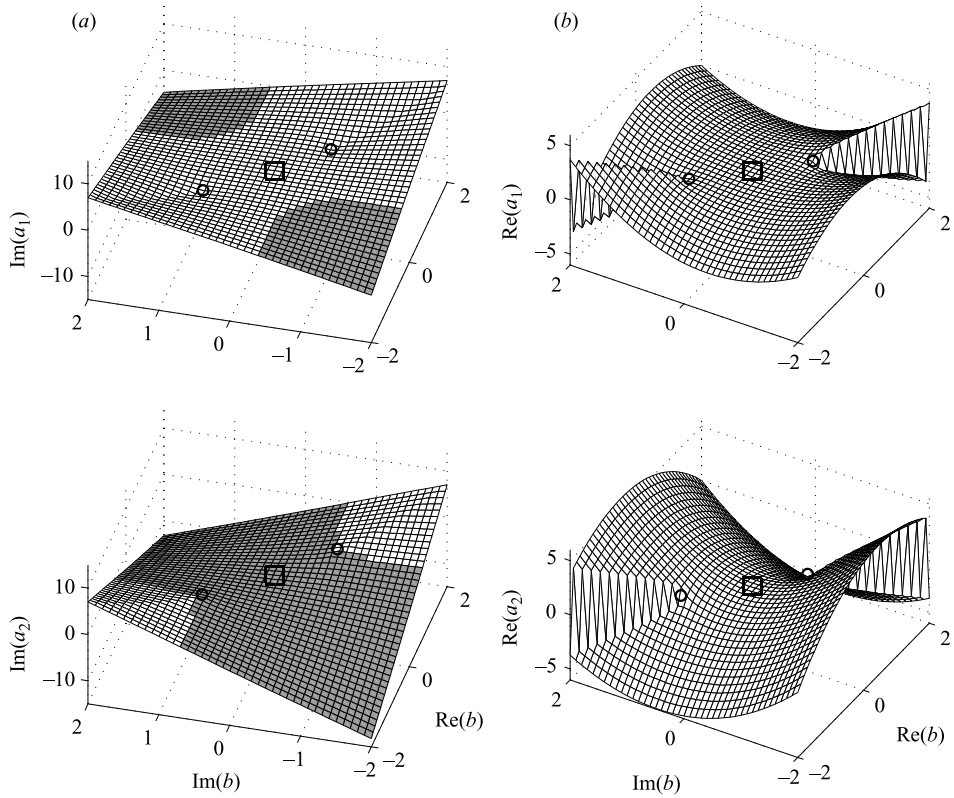


FIGURE 10. (a) Imaginary and (b) real parts of  $a_1(b)$  (top figures) and  $a_2(b)$  (bottom figures) including branch points  $\partial_a \omega = 0$  ( $\circ$ ) and  $\partial_b \omega = 0$  with  $b = 0$  ( $\square$ ) for  $r - \rho^2 = -1$ ,  $r^t - \rho^2 = 1$ ,  $\rho = 0.175$ , and  $c$  and  $\eta$  as given in §4. The regions of negative imaginary part are shown in a darker shade.

a function of  $a$ :

$$b_{\pm, \pm} = \pm \left( -a - \frac{1}{2} i \rho \eta \pm \left( \frac{1}{4} \rho^2 ((c + \eta)^2 - \eta^2) - (r^t - r) - i \rho c a \right)^{1/2} \right)^{1/2}. \quad (5.4)$$

As (2.7) is second order in  $b^2$ , a choice of branch cut for the root of  $b^2$  along the positive real  $b$ -axis produces two solutions with  $\text{Im}(b) > 0$  and two other solutions with  $\text{Im}(b) < 0$ . These four solution surfaces are connected at four branch points given by  $\partial_b \omega = 0$ :

$$a_{\text{bp3}} = -i \left( \frac{\rho}{2} (c + \eta) + (r^t - r)^{1/2} \right), \quad (5.5a)$$

$$b_{\text{bp3}} = 0, \quad (5.5b)$$

$$a_{\text{bp4}} = -i \left( \frac{\rho}{2} (c + \eta) - (r^t - r)^{1/2} \right), \quad (5.6a)$$

$$b_{\text{bp4}} = 0, \quad (5.6b)$$

$$a_{\text{bp5}} = i \left( \frac{r^t - r}{\rho c} - \frac{\rho^2}{4 \rho c} ((c + \eta)^2 - \eta^2) \right), \quad (5.7a)$$

$$b_{\text{bp5}} = \left( \frac{r^t - r}{2 \rho c} - \frac{\rho c}{8} \right)^{1/2} (1 - i) \quad (5.7b)$$

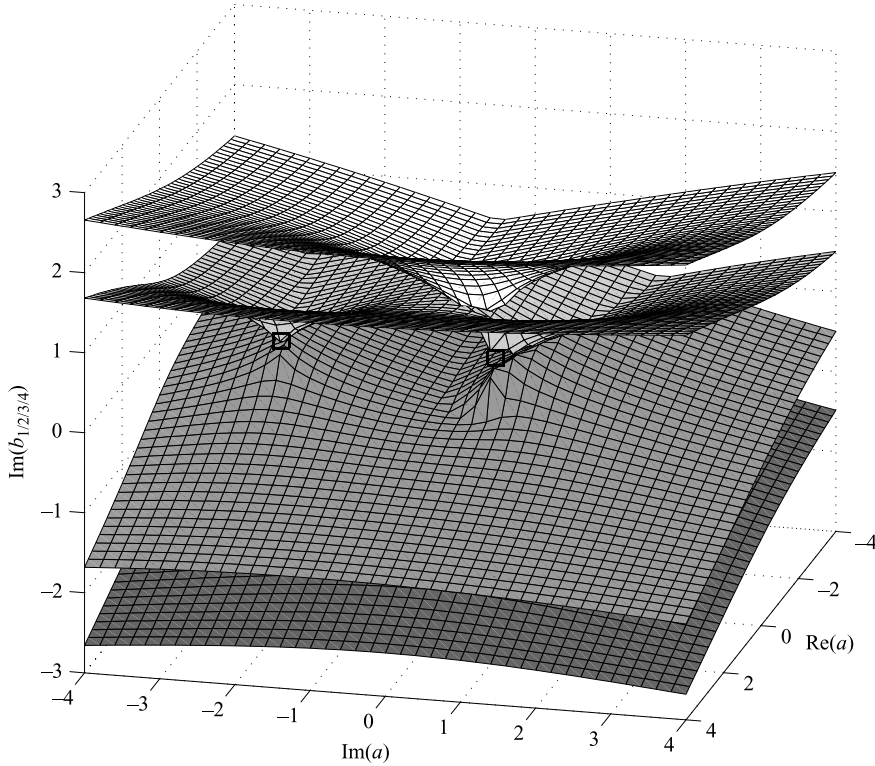


FIGURE 11. Imaginary parts of the four surfaces  $b_1(a)$ – $b_4(a)$  (progressively shaded darker) and branch points for  $\partial_b \omega = 0$  with  $b = 0$  ( $\square$ ). Parameters as in figure 10.

and

$$a_{\text{bp}6} = i \left( \frac{r^t - r}{\rho c} - \frac{\rho^2}{4\rho c} ((c + \eta)^2 - \eta^2) \right), \tag{5.8a}$$

$$b_{\text{bp}6} = - \left( \frac{r^t - r}{2\rho c} - \frac{\rho c}{8} \right)^{1/2} (1 - i). \tag{5.8b}$$

Proceeding now to the branch cuts in the  $a$ -plane, they are again chosen along Stokes lines which allows us to sort the solutions  $b$ , for all  $a$ , according to their imaginary parts

$$\text{Im}(b_1) > \text{Im}(b_2) > 0 > \text{Im}(b_3) > \text{Im}(b_4), \tag{5.9}$$

as depicted in figure 11. These Stokes lines in the  $a$ -plane are defined by  $\text{Im}(b_{+,+}) = \text{Im}(b_{+,-})$  and  $\text{Im}(b_{-,-}) = \text{Im}(b_{-,+})$ . They are determined implicitly by the relation (5.9) since no analytical representation has been found for them. Nevertheless, it follows from (5.5)–(5.8) that the surfaces  $b_2$  and  $b_3$  are connected by the branch points  $a_{\text{bp}3}$  and  $a_{\text{bp}4}$  with  $b(a) = 0$ .

When choosing the appropriate root of  $b$ , we are faced with the additional difficulty that, even if the imaginary parts did not change sign on any solution surface, there are for each sign two roots of  $b$  to choose from. Hence, the sign of the imaginary part is again not a sufficient criterion for the correct choice of the branch of  $b$ . By considering specific paths joining different regions of physical space in figure 1

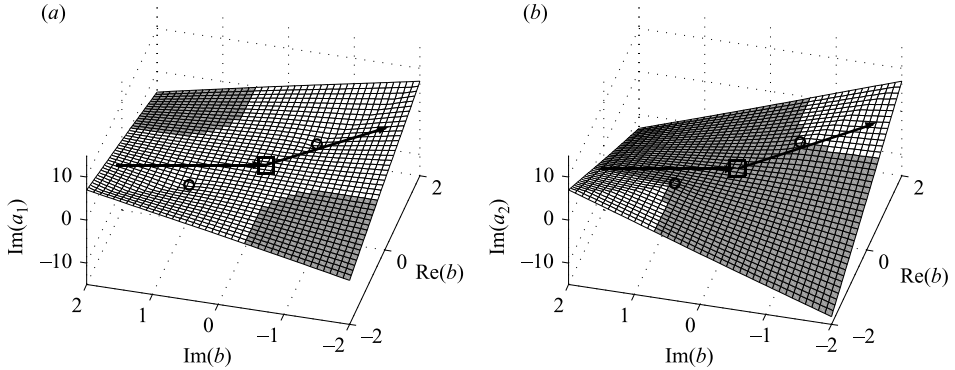


FIGURE 12. Imaginary parts of the two surfaces (a)  $a_1(b)$  and (b)  $a_2(b)$  including branch points  $\partial_a \omega = 0$  ( $\circ$ ) and  $\partial_b \omega = 0$  with  $b = 0$  ( $\square$ ). Parameters and conventions (regions of  $\text{Im}(a) < 0$  shown in darker shade) as in figure 10. On both branches, a path joining the  $(\text{Im}(a) > 0, \text{Im}(b) < 0)$  and  $(\text{Im}(a) > 0, \text{Im}(b) > 0)$  regions is shown schematically.

(related to regions of wavenumber space by virtue of 2.10), the proper choice of  $a$ - and  $b$ -branches can nevertheless be specified.

Consider for instance a path connecting in Fourier space the  $(\text{Im}(a) > 0, \text{Im}(b) < 0)$  and  $(\text{Im}(a) > 0, \text{Im}(b) > 0)$  regions of figure 1 sufficiently far from the inner region such that  $r \approx r_\infty$  along the entire path. If this path crosses a region in Fourier space where the imaginary part of  $a$  is negative, the growth factor  $\exp(-\text{Im}(a) X/\varepsilon)$  in this region becomes exponentially large as the path is shifted toward  $X \rightarrow +\infty$ . With the path on the  $a_2$  branch, such a region of  $\text{Im}(a) < 0$  exists around the point  $b = 0$ , which has to be crossed to change the sign of the imaginary part of  $b$  (see figure 12b). It is thus clear that  $\text{Im}(a) < 0$  can only be avoided by a path on the  $a_1$ -surface, which is therefore the relevant  $a$ -branch for  $X \rightarrow +\infty$  (see figure 12a). Similarly,  $a_2$  is the relevant branch for  $X \rightarrow -\infty$ .

Next, two paths connecting the  $(\text{Im}(a) < 0, \text{Im}(b) < 0)$  and  $(\text{Im}(a) > 0, \text{Im}(b) > 0)$  regions of figure 1 are considered, one staying in remote regions where  $r - \rho^2 \approx -1$  with a detour through the  $(\text{Im}(a) < 0, \text{Im}(b) > 0)$  region, the other going directly through the two-dimensional double turning point at the origin where  $r - \rho^2 \approx 1$ . In order to have a uniquely defined phase, these two paths have to end up on the same wavenumber branches.

As seen in figure 13, the shape of the solution surfaces  $a_1$  and  $a_2$  is only slightly modified with regard to  $r$ . The main difference between figures 13(a) ( $r - \rho^2 = 1$ ) and 13(b) ( $r - \rho^2 = -1$ ) is in (a) the complete separation of the surfaces by the branch cuts originating from the branch points  $(a_{\text{bp}1}, b_{\text{bp}1})$ ,  $(a_{\text{bp}2}, b_{\text{bp}2})$ ,  $(a_{\text{bp}3}, b_{\text{bp}3})$  and  $(a_{\text{bp}4}, b_{\text{bp}4})$  which all coalesce at  $b = 0$ . The first path through the two-dimensional turning point at  $b = 0$  shown in figure 13(a) switches from the  $a_2$ - to the  $a_1$ -branch and from a  $b$ -branch with  $\text{Im}(b) < 0$  to a  $b$ -branch with  $\text{Im}(b) > 0$ . Considering that only the surfaces  $b_2$  and  $b_3$  are connected by branch points which merge into the two-dimensional turning point at the coordinate origin as  $r \rightarrow r^*$  and that  $\text{Im}(b_2) > 0 > \text{Im}(b_3)$  by virtue of relation (5.9), the relevant branches of  $b$  far from the central region are  $b_2$  for  $Y \rightarrow \infty$  and  $b_3$  for  $Y \rightarrow -\infty$ . Hence, the same branch switches occur on the two paths in figure 13 as required.

In summary, the determination of the physically relevant solution surfaces is guided by three conditions: the first condition specifies the sign of the imaginary parts of the two wavenumbers to make certain that the global mode is locally stable far from the

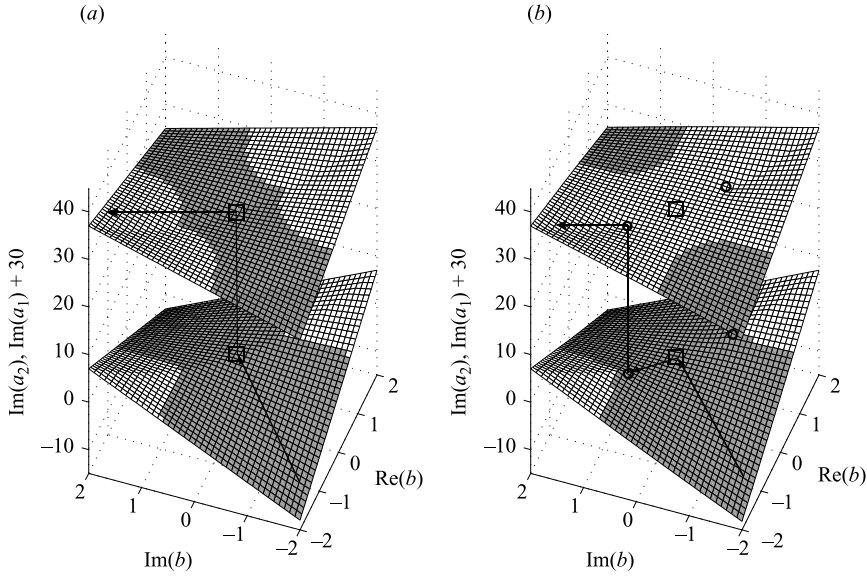


FIGURE 13. Imaginary parts of the two surfaces  $a_1(b)$  and  $a_2(b)$  including branch points  $\partial_a \omega = 0$  ( $\circ$ ) and  $\partial_b \omega = 0$  with  $b = 0$  ( $\square$ ) for (a)  $r - \rho^2 = 1$  and (b)  $r - \rho^2 = -1$ . The surface  $\text{Im}(a_1)$  is arbitrarily shifted upward for the sake of clarity. The other parameters and conventions as in figure 10. Also shown are the paths connecting the  $(\text{Im}(a) < 0, \text{Im}(b) < 0)$  and  $(\text{Im}(a) > 0, \text{Im}(b) > 0)$  regions via the two-dimensional turning point (a) and via the  $(\text{Im}(a) < 0, \text{Im}(b) > 0)$  region (b).

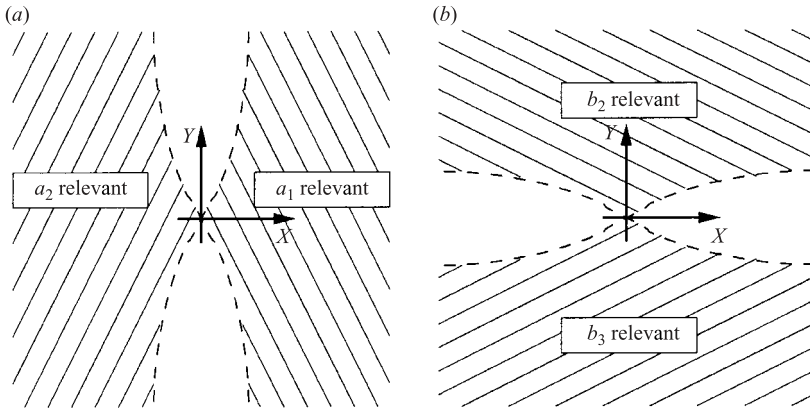


FIGURE 14. Relevant branches of (a)  $a$  and (b)  $b$  in physical space. The domains of relevance are bounded by dashed lines, which merge at the two-dimensional double turning point.

central region, as sketched in figure 1. The second condition specifies that only the branches of the dispersion relation connected by branch points which coalesce into the two-dimensional double turning point are relevant. This ensures that the branch switches on different paths in physical space, as depicted in figure 13, are consistent. The last condition specifies that adjacent regions with the same sign of  $\text{Im}(a)$  or  $\text{Im}(b)$  must be connectible in Fourier space by a path along which this sign never changes, as shown in figure 12(a). These three conditions yield the diagram in figure 14, from whom the analytical expressions of the relevant solution surfaces can be deduced.

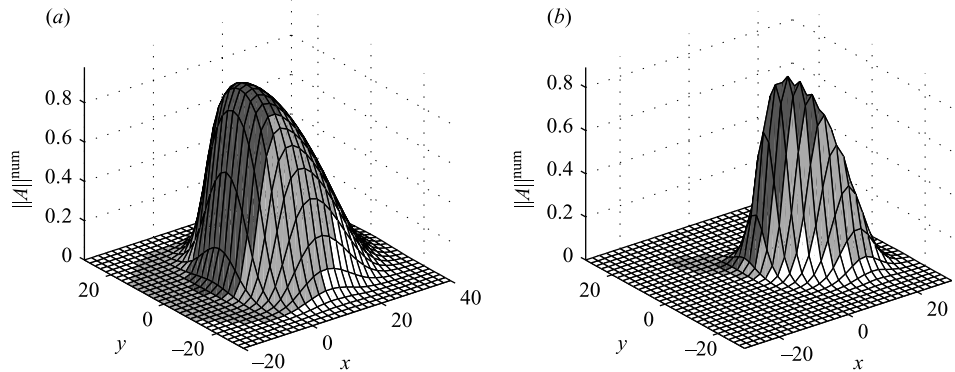


FIGURE 15. Nonlinear evolution at  $t=300$  of the envelope of the numerical simulations. (a) Extension of figure 5(c) with the same parameters and conventions. (b) Analogous extension of figure 8(c).

The next step in evaluating the leading-order WKB expansion in the entire  $(X, Y)$ -space would be the practical determination of the fields  $a(x, y)$  and  $b(x, y)$ , where the location of the branch points in the  $(X, Y)$ -space is known from their dependence on  $r(X, Y)$ . This complex task is still open. Another open question concerns the nonlinear saturation of these global modes. Nonlinear modes have been numerically observed and studied by Müller, Lücke & Kamps (1992) and Couairon & Chomaz (1997) in homogeneous systems of finite size. In the present problem, the inhomogeneity is distributed and not as abrupt as that provided by boundaries. Hence, the inhomogeneous system considered here is rather the two-dimensional extension of the situation in Pier *et al.* (2001). Their nonlinear ‘elephant’ global modes exhibit a front located at the upstream LCU/LAU boundary, which selects the pulsation and wavenumber of the instability. In our numerical simulations in which the cubic nonlinearity saturates the instability, we observe a qualitatively similar behaviour, as seen in figure 15. Nevertheless, a two-dimensional equivalent of their nonlinear selection criterion is, at this point, far from obvious.

In conclusion, it is important to emphasize that the integration of the outer WKB expansion and the selection criterion of the linear global mode are independent issues. As it stands, the latter is self-consistent and has been used successfully to determine the critical conditions of inhomogeneous Rayleigh–Bénard–Poiseuille convection by an envelope equation formalism. This methodology should also be useful for the stability analysis of other inhomogeneous systems with supercritical behaviour.

The financial support of the ERCOFTAC Leonhard Euler Center, the Direction des Relations Internationales of the CNRS (Ph. C.) and the DERTT of the Région Rhône-Alpes (D. M.) is gratefully acknowledged. We also would like to thank J. F. Scott for several helpful discussions.

#### REFERENCES

- ABRAMOVITZ, M. & STEGUN, I. A. 1964 *Handbook of Mathematical Functions with Formulas, Graphs and Mathematical Tables*. National Bureau of Standards.
- ALBARÈDE, P. & MONKEWITZ, P. A. 1992 A model for the formation of oblique shedding and ‘chevron’ patterns in cylinder wakes. *Phys. Fluids A* **4**, 744–756.

- CARRIÈRE, P. & MONKEWITZ, P. A. 2001 Transverse-roll global modes in a Rayleigh–Bénard–Poiseuille system with streamwise variable heating. *Eur. J. Mech. B/Fluids* **20**, 751–770.
- CARRIÈRE, P., MONKEWITZ, P. A. & MARTINAND, D. 2004 Envelope equations for the Rayleigh–Bénard–Poiseuille system. Part 1. Spatially homogeneous case. *J. Fluid Mech.* **502**, 153–174.
- CHOMAZ, J.-M., HUERRE, P. & REDEKOPP, L. G. 1991 A frequency selection criterion in spatially developing flows. *Stud. App. Maths* **84**, 119–144.
- COUAIRON, A. & CHOMAZ, J.-M. 1997 Absolute and convective instabilities, front velocities and global modes in nonlinear systems. *Physica D* **108**, 236–276.
- CRIGHTON, D. & GASTER, M. 1976 Stability of slowly diverging jet flow. *J. Fluid Mech.* **77**, 397–413.
- GASTER, M., KIT, E. & WYGNANSKI, I. 1985 Large-scale structures in a forced turbulent mixing layer. *J. Fluid Mech.* **150**, 23–39.
- HUERRE, P. & MONKEWITZ, P. A. 1990 Local and global instabilities in spatially developing flows. *Annu. Rev. Fluid Mech.* **22**, 473–537.
- LE DIZÈS, S., HUERRE, P., CHOMAZ, J.-M. & MONKEWITZ, P. A. 1996 Linear global modes in spatially developing media. *Phil. Trans. R. Soc. Lond. A* **354**, 169–212.
- MARTINAND, D. 2003 Détermination analytique des modes globaux tridimensionnels en écoulement de convection mixte du type Rayleigh–Bénard–Poiseuille. PhD thesis, Université Claude Bernard Lyon I.
- MONKEWITZ, P. A., HUERRE, P. & CHOMAZ, J.-M. 1993 Global linear stability analysis of weakly non-parallel shear flows. *J. Fluid Mech.* **288**, 1–20.
- MÜLLER, H. W., LÜCKE, M. & KAMPS, M. 1992 Transversal convection patterns in horizontal shear flow. *Phys. Rev. A* **45**, 3714–3726.
- PIER, B., HUERRE, P. & CHOMAZ, J.-M. 2001 Bifurcation to fully nonlinear synchronized structures in slowly varying media. *Physica D* **148**, 49–96.
- POLYANIN, A. D. & ZAITSEV, V. F. 1995 *Handbook of Exact Solutions for Ordinary Differential Equations*. CRC Press, Boca Raton, Florida.